
FibQuant: Universal Vector Quantization for Random-Access KV-Cache Compression

Namyoon Lee
POSTECH
nylee@postech.ac.kr

Yongjune Kim
POSTECH
yongjune@postech.ac.kr

Abstract

Long-context inference is increasingly a memory-traffic problem. The culprit is the key-value (KV) cache: it grows with context length, batch size, layers, and heads, and it is read at every decoding step. A useful cache codec is therefore not merely a quantizer. It is also a data structure: every cached key and value must occupy a fixed address and be reconstructed independently, so decompression can be fused with attention. Rotation-based scalar codecs meet this systems constraint by storing a norm, applying a shared random rotation, and quantizing one coordinate at a time. They are universal and random-access, but they discard the geometry created by the normalization step. After a Haar rotation, a block of k consecutive coordinates is not a product source; it is a spherical-Beta source on the unit ball. We introduce FIBQUANT, a universal fixed-rate vector quantizer that keeps the same normalize-rotate-store interface while replacing scalar tables by a shared radial-angular codebook matched to this canonical source. The codebook combines Beta-quantile radii, Fibonacci/Roberts-Kronecker quasi-uniform directions, and multi-restart Lloyd-Max refinement. We prove that the resulting vector code strictly improves on its scalar product specialization at matched rate, with a high-rate gain that separates into a cell-shaping factor and a density-matching factor. The same construction gives a dense rate axis, including fractional-bit and sub-one-bit operating points, without calibration or variable-length addresses. On GPT-2 small KV caches, FIBQUANT traces a memory-fidelity frontier from $5\times$ compression at 0.99 attention cosine similarity to $34\times$ at 0.95. End-to-end on TinyLlama-1.1B, it is within 0.10 perplexity of fp16 at $4\times$ compression and has $3.6\times$ lower perplexity than scalar TURBOQUANT at $b = 2$ ($8\times$ compression), where scalar random-access quantization begins to fail.

1 Introduction

The key-value (KV) cache is the state carried by an autoregressive transformer. Its size grows linearly with context length, batch size, layer count, and head count; its contents are accessed at every decoding step. In long-context serving, the cache is therefore not an auxiliary buffer. It is often the object that determines memory bandwidth, batch size, and latency, and in extreme regimes it can exceed the model weights itself [1]. This pressure has led to two-bit and lower-precision cache quantization methods such as KIVI and KVQUANT [2, 3].

The cache, however, imposes a constraint that is absent from ordinary source coding. A deployable cache codec must be *random-access*: the representation of token t must live at a fixed address, and the corresponding key or value must be decoded independently by simple address arithmetic. Otherwise decompression cannot be fused with the attention kernel [1]. This single constraint explains why fixed-rate quantizers dominate the source-coding layer of KV-cache compression [2, 3, 6, 7]. It rules out many statistically attractive variable-length or context-dependent representations before one even asks about distortion.

The cleanest representative of this random-access family is TURBOQUANT [6]. It stores the vector norm, applies a shared random orthogonal rotation, and quantizes each rotated coordinate with the same scalar Lloyd–Max table. This is the right *interface*: source-agnostic, fixed-rate, and easy to fuse. But it is the wrong *geometry*. Once a vector has been normalized and Haar-rotated, a block of k consecutive coordinates lies on the unit ball with a specific radial law and a uniform angular component. The coordinates are not an independent product of shifted-Beta marginals. A scalar code sees one coordinate at a time; the source seen by the cache is intrinsically vectorial.

The sub-one-bit gap. In production, the admissible cache rate is not chosen by an elegant integer-bit quantizer. It is set by VRAM, latency, context length, and batch size. When this budget falls below roughly one bit per coordinate, current universal, calibration-free, random-access codecs cease to operate: TURBOQUANT bottoms out at one bit, RABITQ [7] is a one-bit signed code, and KIVI/KVQUANT primarily target two bits or above. The remaining alternatives either rely on calibration, as in low-rank projection methods such as PALU [13], or alter the sequence itself through eviction or retention policies such as STREAMINGLLM and H2O [10, 9]. The missing object is a fixed-rate, calibration-free, random-access codec with a continuously tunable rate axis below one bit per coordinate.

Contribution. We ask a simple question: *what is the canonical source induced by the random-access normalize–rotate interface?* The answer is the spherical-Beta law $f_{d,k}$ on the unit ball \mathbb{B}^k . Once this law is identified, the rest of the codec is classical. The radius is matched by Bennett–Gersho companding, the direction by quasi-uniform spherical point sets, and the finite-rate codebook by Lloyd–Max refinement. The result is FIBQUANT: a vector quantizer that keeps the serving interface of scalar rotation codes but recovers the shaping and density-matching gains that scalar products leave on the table.

Our contributions are as follows.

- **Canonical source.** We prove that norm-then-Haar-rotation maps every nonzero input distribution to the same k -block marginal $f_{d,k}$ on \mathbb{B}^k (Theorem 1). Thus one shared offline codebook is the correct universal object for layers, heads, prompts, and models.
- **Vector advantage.** We show that the best k -vector code strictly dominates the scalar product specialization at matched rate, and that the high-rate gain factors into a cell-shaping term and a density-matching term (Theorem 2).
- **Dense rate axis.** Because the rate is $b = (\log_2 N)/k$, FIBQUANT realizes fractional-bit and sub-one-bit operating points while preserving fixed addresses and independent decoding (Figure 3).
- **KV-cache evidence.** On GPT-2 small, FIBQUANT reaches $34.1\times$ compression at 0.946 attention-output cosine similarity, the only universal random-access method in our comparison beyond $10\times$ compression (Figure 4). On TinyLlama-1.1B, it strictly dominates per-token INT and scalar TURBOQUANT at matched integer rates on WikiText-103 perplexity and HellaSwag accuracy (Sec. 5.3).

2 Background and Related Work

FIBQUANT is a source-coding layer for a specific systems interface: fixed-rate random access to cached keys and values. It is therefore complementary to eviction, low-rank projection, and fused-kernel systems work. We separate the related work according to this role.

KV-cache compression. Existing approaches reduce the KV cache along different axes. Quantizers reduce precision, from outlier-aware matrix quantization such as LLM.INT8() [14] to cache-specific methods such as KIVI, KVQUANT, GEAR, and QJL [2, 3, 4, 5]. Token-selection methods reduce the sequence dimension by keeping attention sinks or heavy hitters [10, 9, 11, 12]. Low-rank methods such as PALU exploit calibrated head-specific subspaces [13]. System frameworks such as KVCOMP focus on making compression compatible with the memory hierarchy and the attention kernel [1]. These methods attack different bottlenecks. Our question is narrower and more primitive: *given a random-access fixed-rate cache slot, what source code should occupy it?*

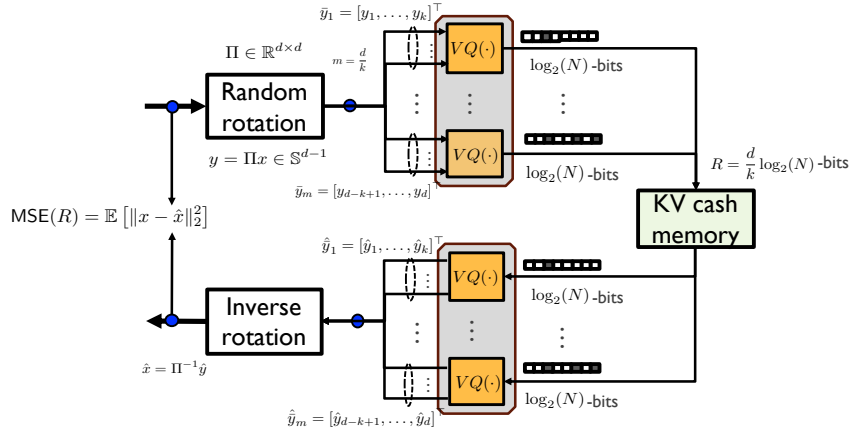


Figure 1: **FIBQUANT encoder-decoder pipeline.** A cached vector $x \in \mathbb{R}^d$ is split into a scalar norm header $\nu = \|x\|_2$ and a unit direction $\Pi x/\nu$, where $\Pi \in \mathbb{R}^{d \times d}$ is a single Haar-random orthogonal matrix shared across layers, heads, prompts and tokens. The unit direction is partitioned into d/k blocks of k consecutive coordinates, each falling on the unit ball \mathbb{B}^k with marginal density $f_{d,k}$ (Lemma 1). Each block is encoded to one of N indices by nearest-codeword lookup against the shared offline codebook $\mathcal{C} = \{c_n\}_{n=1}^N$ (Eq. (1)); the decoder reverses the lookup and the rotation to recover \hat{x} . The output bitstream is a fixed-rate $(d \log_2 N)/k$ -bit payload plus one fp16 norm per cached vector, so token slots are at affine offsets and any past key/value can be recovered independently—the random-access requirement that distinguishes deployable cache codecs from variable-length alternatives. The only change from TURBOQUANT’s pipeline is the replacement of the per-coordinate scalar table by one k -dimensional vector quantizer.

Rotation-then-quantize codes. The closest prior art is the family of source-agnostic rotation codes. TURBOQUANT stores a norm, applies a shared random rotation, and quantizes each rotated coordinate using a Lloyd–Max table matched to the shifted-Beta scalar marginal [6]. RABITQ reaches an analogous universality principle for approximate nearest-neighbor search through a one-bit signed code with a sharp distance bound [7]; a recent comparison studies these two views side by side [8]. These methods identify the correct deployment interface. The difference is that they stop at scalar marginals. FIBQUANT applies the same interface to k -blocks, where the induced law is the spherical-Beta vector distribution rather than a product of scalar marginals. This single change yields a dense rate axis and the vector-quantization gains proved in Sec. 4.

Spherical vector quantization. The codebook geometry uses classical ingredients. The planar Fibonacci spiral at $k = 2$ is related to the Golden Quantizer for a complex Gaussian source [26], Fibonacci-lattice color quantization [27], and sunflower antenna arrays [28]. Higher-dimensional directions use Fibonacci-sphere and Roberts–Kronecker low-discrepancy constructions [22, 23, 24, 20, 21], and the refinement step is the Lloyd–Max / Gersho theory of vector quantization [15, 16, 17, 18, 19]. What is new here is not any one geometric primitive. It is the matching of those primitives to the spherical-Beta source forced by random-access KV-cache compression.

3 Model and Codec

Overview. The codec has three parts. First, every cached vector is normalized and rotated by a shared Haar-random orthogonal matrix. This is the same random-access interface used by scalar rotation codes: the norm is a small side header, the payload is fixed length, and every token can be decoded independently. Second, the rotated unit vector is partitioned into k -dimensional blocks. Lemma 1 shows that each block has the same spherical-Beta density $f_{d,k}$ on the unit ball, independent of the original KV distribution. Third, a shared offline codebook $\mathcal{C} = \{r_n u_n\}_{n=1}^N$ is built for this density: Beta-quantile radii r_n , quasi-uniform directions u_n , and a multi-restart Lloyd–Max polish. The encoder performs nearest-codeword lookup per block; the decoder performs table lookup and inverse rotation.

The point is deliberately conservative. FIBQUANT changes the statistical object being quantized, not the serving contract. The bitstream remains fixed-rate and randomly addressable; only the scalar coordinate table is replaced by a vector codebook matched to the law that the interface itself creates.

The section proceeds in three steps: the encoder–decoder pair (Sec. 3.1), the canonical source law (Sec. 3.2), and the radial–angular codebook construction (Sec. 3.3).

3.1 Random-access vector encoding

Fix one attention head of width d , a shared orthogonal matrix $\Pi \in \mathbb{R}^{d \times d}$, and a codebook $\mathcal{C} = \{c_1, \dots, c_N\} \subset \mathbb{B}^k$ with $k \mid d$. For a nonzero cached vector $x \in \mathbb{R}^d$, the encoder stores the fp16 norm header $\nu = \|x\|_2$ and quantizes the rotated unit vector $\Pi x/\nu$. Write its block decomposition as $\Pi x/\nu = (y^{(1)}, \dots, y^{(d/k)})$, with $y^{(m)} \in \mathbb{B}^k$. The stored index for block m is

$$i_m = \arg \min_{1 \leq j \leq N} \|y^{(m)} - c_j\|_2^2, \quad m = 1, \dots, d/k. \quad (1)$$

The decoder sets $\hat{y}^{(m)} = c_{i_m}$ and returns $\hat{x} = \nu \Pi^\top \hat{y}$. The payload rate is $b = (\log_2 N)/k$ bits per coordinate, identical for every vector and every token. Hence token addresses are affine in the time index, and random access is preserved by construction.

Loss functions. We track two losses. The intrinsic source-coding loss is

$$\mathcal{L}_{\text{mse}}(\mathcal{C}) = \mathbb{E} \sum_{m=1}^{d/k} \min_j \|Y^{(m)} - c_j\|_2^2, \quad (2)$$

where $Y^{(m)}$ is distributed according to the canonical law $f_{d,k}$ derived in Sec. 3.2. The downstream metric is attention-output cosine similarity,

$$\mathcal{L}_{\text{attn}}(\mathcal{C}) = \mathbb{E}_{\ell,h,q} \frac{\langle o_{\ell,h}(q), \hat{o}_{\ell,h}(q) \rangle}{\|o_{\ell,h}(q)\| \|\hat{o}_{\ell,h}(q)\|}, \quad o_{\ell,h}(q) = \text{softmax}\left(\frac{qK_{\ell,h}^\top}{\sqrt{d}}\right) V_{\ell,h}, \quad (3)$$

with $\hat{o}_{\ell,h}$ computed from the reconstructed $\hat{K}_{\ell,h}, \hat{V}_{\ell,h}$. A task-weighted or Mahalanobis Lloyd objective can be used offline by replacing $\|x - c\|_2^2$ with $(x - c)^\top M_h(x - c)$; the random-access bitstream and decoder are unchanged.

3.2 The canonical vector source

The normalization removes scale; the Haar rotation removes orientation. Consequently the distribution seen by the block quantizer is universal. Let $\bar{x} = x/\|x\|$. Conditional on any fixed direction $\bar{x} = v$, Πv is Haar-uniform on the unit sphere \mathbb{S}^{d-1} by rotational invariance. Averaging over v does not change this law. Thus every input distribution with $\Pr(X = 0) = 0$ induces the same rotated unit-vector law. The k -block marginal is the following spherical-Beta density.

Lemma 1 (Spherical-Beta vector marginal). *Let $U \sim \text{Unif}(\mathbb{S}^{d-1})$ and $X = U_{1:k}$ for $1 \leq k < d$. Then X has density $f_{d,k}(x) = C_{d,k}(1 - \|x\|^2)^{(d-k-2)/2} \mathbf{1}\{\|x\| \leq 1\}$ on \mathbb{B}^k , with*

$$R^2 \sim \text{Beta}(k/2, (d-k)/2), \quad \mathbb{E}R^2 = k/d, \quad \text{Var}(R^2) = \frac{2k(d-k)}{d^2(d+2)}, \quad (4)$$

and X/R uniform on \mathbb{S}^{k-1} , independent of R .

At $k = 1$, Lemma 1 reduces to the shifted-Beta scalar marginal used by scalar TURBOQUANT. For $k > 1$, however, the joint law is not the product of those marginals. This distinction is the whole source of the vector gain: scalar quantization is matched to one-coordinate projections, while the cache interface naturally exposes blocks with radial–angular structure.

Two consequences guide the design.

- (P1) *Stationarity after rotation.* Every block $Y^{(m)}$ has density $f_{d,k}$ on \mathbb{B}^k , independent of layer, head, prompt, token, and the original KV distribution. A single shared codebook is therefore a universal offline object.

(P2) Concentration on a shell. Since $\text{Var}(R^2) = O(d^{-2})$, high-dimensional mass concentrates near $\bar{R} = \sqrt{k/d}$. At large d , the problem becomes primarily one of placing directions on \mathbb{S}^{k-1} ; at moderate d , the residual radial spread is captured by Beta-quantile radii.

3.3 Radial–angular codebook construction

Lemma 1 factorizes the design problem. Each codeword is written as $c_n = r_n u_n$, with radius $r_n \in [0, 1]$ and direction $u_n \in \mathbb{S}^{k-1}$. The radii match the radial density of the spherical-Beta source; the directions approximate a uniform spherical packing; Lloyd–Max refinement then adapts the deterministic initialization to the finite value of N .

Radii. Bennett’s high-rate companding rule, in its vector-quantization form due to Gersho [17], places codewords with density proportional to $f_{d,k}^{k/(k+2)}$ for MSE. Specializing this rule to the radius gives a Beta law with shape $(k/2, \beta_{d,k})$. Midpoint quantiles $q_n = (n - \frac{1}{2})/N$ yield

$$r_n = \sqrt{\text{BetaInv}(q_n; \frac{k}{2}, \beta_{d,k})}, \quad \beta_{d,k} = \frac{k}{k+2} \cdot \frac{d-k-2}{2} + 1. \quad (5)$$

For $k = 2$, this inverse is closed form:

$$r_n = \sqrt{1 - (1 - q_n)^{4/d}}. \quad (6)$$

Directions. The direction set $\{u_n\}_{n=1}^N \subset \mathbb{S}^{k-1}$ is chosen by geometry, not by calibration data:

- $k = 2$: a planar Fibonacci spiral, $u_n = (\cos \theta_n, \sin \theta_n)$ with $\theta_n = 2\pi(n-1)\theta_g$ and $\theta_g = 1 - 1/\varphi$.
- $k = 3$: a Fibonacci sphere with equal-area latitude bands and golden-angle azimuth; the multi-shell variant is given in Appendix E.
- $k \geq 4$: a Roberts–Kronecker rank-one sequence $\xi_{n,j} = \{(n - \frac{1}{2})\phi_k^{-j}\}$, where ϕ_k is the positive root of $\phi^{k+1} = \phi + 1$, mapped through Φ^{-1} and projected onto \mathbb{S}^{k-1} .

Lloyd–Max refinement. The deterministic initialization $c_n^{(0)} = r_n u_n$ is refined on samples from $f_{d,k}$. Each restart applies a random orthogonal rotation to the initial codebook, alternates nearest-neighbor assignment and centroid update, repairs empty cells by splitting high-distortion cells, and keeps the codebook with the lowest training MSE. The full procedure is specified in Appendix A, Table 2. This refinement is offline metadata: it does not alter the fixed-rate payload or the random-access decoder.

3.4 Example: $k = 2$

The two-dimensional case shows the construction in closed form. Here $\beta_{d,2} = d/4$, so (5) becomes (6). Combining these radii with the golden-angle sequence gives the sunflower initialization $c_n^{(0)} = r_n(\cos \theta_n, \sin \theta_n)$, $n = 1, \dots, N$, followed by the same Lloyd–Max polish used in all dimensions.

Figure 2 shows the result for $N \in \{8, 16, 32, 64\}$ and $d \in \{16, 128\}$. At $d = 16$, the spherical-Beta density has visible radial spread, and the codewords use several radii. At $d = 128$, the mass has nearly collapsed onto the shell $\bar{R} = \sqrt{2/d} \approx 0.125$, and the problem becomes mostly angular. Along that shell, the Lloyd-polished cells approach the hexagonal geometry expected of an efficient two-dimensional vector quantizer. This picture is the finite-dimensional version of Theorem 2: a scalar product code can tile the plane by rectangles, but it cannot recover the shaping gain of these cells.

The same effect appears quantitatively in Figure 3. At integer rates, the $k = 2$ branch lies below scalar TURBOQUANT; at fractional rates, the same codebook family gives operating points that scalar Lloyd–Max cannot realize at all.

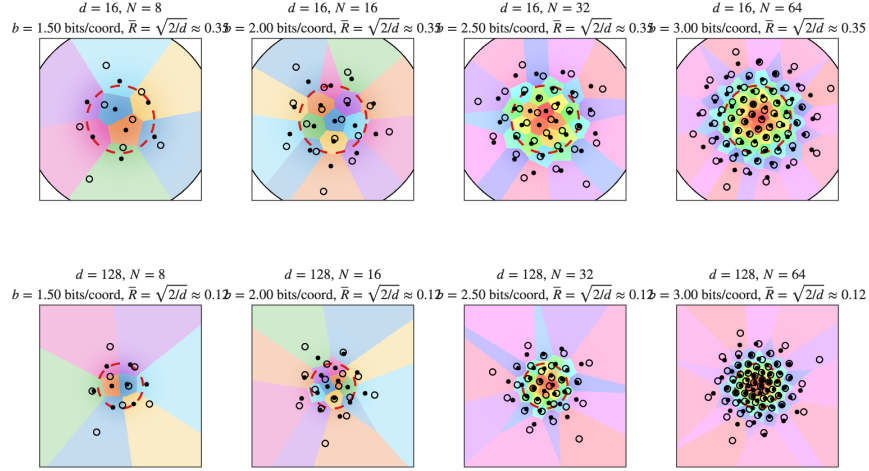


Figure 2: FIBQUANT $k = 2$ codebooks and their Voronoi cells on \mathbb{B}^2 at $d = 16$ (top row) and $d = 128$ (bottom row), for $N \in \{8, 16, 32, 64\}$. Open markers: Beta-quantile + Fibonacci init. Solid markers: codewords after Lloyd–Max. Background heat-map: spherical-Beta source density $f_{d,2}$. Discussion in Sec. 3.4.

4 Analysis

The analysis formalizes the message of the construction. Random access fixes the source; the source fixes the correct codebook; vector quantization then improves on the scalar product restriction.

Theorem 1 (Source-agnostic universality). *Let X be any random vector in \mathbb{R}^d with $\Pr(X = 0) = 0$, independent of a Haar-uniform orthogonal Π , and let $Y = \Pi X / \|X\|$. Then Y is Haar-uniform on \mathbb{S}^{d-1} , and every k -coordinate vector of Y has marginal density $f_{d,k}$.*

Proof. Condition on $X / \|X\| = v$. By invariance of Haar measure, Πv is uniform on \mathbb{S}^{d-1} . Averaging over v leaves the Haar law unchanged. Lemma 1 gives the k -coordinate marginal. \square

The theorem is the universality statement. It says that the shared codebook is not a heuristic trained on a convenient model; it is the canonical source codebook induced by the serving interface itself.

Theorem 2 (Strict matched-rate dominance). *Let $D_{\text{sc}}(d, b)$ be the per-coordinate distortion of scalar Lloyd–Max quantization of the shifted-Beta marginal $f_{d,1}$ at b bits per coordinate, and let $D_{\text{FQ}}^*(d, k, b)$ be the per-coordinate MSE of the best k -vector code with $N = 2^{bk}$ codewords for $f_{d,k}$. Then*

$$D_{\text{FQ}}^*(d, k, b) < D_{\text{sc}}(d, b), \quad k > 1, b > 0, \quad (7)$$

with equality only in the scalar case $k = 1$. At high rate,

$$\frac{D_{\text{sc}}(d, b)}{D_{\text{FQ}}^*(d, k, b)} \simeq \underbrace{\frac{k G_1}{G_k^*}}_{\gamma_{\text{cell}}(k) \geq 1} \cdot \underbrace{\frac{I_{d,1}(1/3)^3}{I_{d,k}(k/(k+2))^{(k+2)/k}}}_{\gamma_{\text{dens}}(d,k) \geq 1}, \quad (8)$$

where $G_1 = 1/12$, G_k^* is the optimal k -cell normalized second moment, and $I_{d,k}(s) = \int_{\mathbb{B}^k} f_{d,k}^s dx$. The cell factor is strict for $k \geq 2$ [19, 17].

A scalar product code is a feasible k -vector code whose codebook is a Cartesian product of one-dimensional levels. The unrestricted vector code optimizes over a larger class of tessellations, and therefore cannot be worse. Equation (8) separates the gain into two terms. The first is geometric: efficient vector cells beat rectangular boxes. The second is statistical: matching the spherical-Beta density beats matching only its scalar marginals. Numerically, the cell-shaping term alone gives approximately 0.17 dB at $k = 2$, 0.66 dB at $k = 3$, 1.42 dB at $k = 8$, and approaches $10 \log_{10}(\pi e/6) \approx 1.53$ dB as $k \rightarrow \infty$. The density-matching term supplies the additional gain observed in Fig. 3.

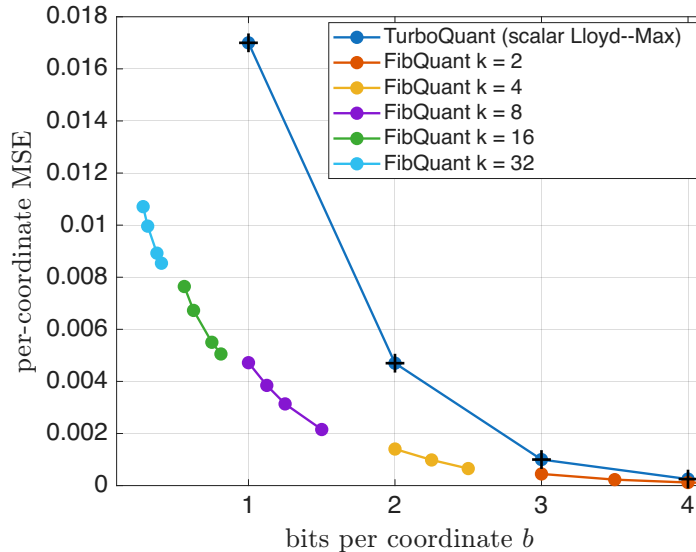


Figure 3: **Per-coordinate MSE versus rate $b = (\log_2 N)/k$ on the canonical spherical-Beta source $f_{d,k}$ at $d = 64$.** Scalar TURBOQUANT (+) contributes only the four integer-bit operating points $b \in \{1, 2, 3, 4\}$, whereas FIBQUANT for $k \in \{2, 4, 8, 16, 32\}$ traces a continuum across the rate axis. Three features are visible. (i) *Strict matched-rate dominance*. At every integer rate the FIBQUANT curve lies strictly below the scalar curve; the vertical gap is the $\gamma_{\text{cell}}(k) \cdot \gamma_{\text{dens}}(d, k)$ factorization of Theorem 2, Eq. (8). (ii) *Fractional-integer-bit coverage*. Between every pair of adjacent integer scalar points FIBQUANT fills the band $b \in \{1.25, 1.5, \dots, 3.5\}$ (annotated arrows) — operating points that no scalar product code can reach. (iii) *Sub-one-bit regime*. Below $b = 1$ FIBQUANT alone operates, all the way down to $b \approx 0.19$ at $(k, N) = (32, 64)$. The $d = 256$ check (omitted here for space) confirms the $1/d$ source-variance scaling of Appendix D.

Full details, including the proof of Lemma 1 and a finite-rate large- d characterization, are given in Appendices B–C.

Rate granularity. Scalar Lloyd–Max tables offer integer-bit operating points. In contrast,

$$\mathcal{B}_{\text{FQ}} = \{(\log_2 N)/k : k, N \in \mathbb{Z}\} \quad (9)$$

is dense in $(0, \infty)$. Thus the rate can be selected after the serving budget is known, including sub-one-bit and fractional-bit regimes, without changing the random-access interface.

5 Experiments

The experiments test three questions. First, does the vector geometry predicted by Theorem 2 reduce source distortion on the canonical spherical-Beta law? Second, does this reduction survive in a real KV cache, where the relevant metric is attention-output fidelity rather than raw MSE? Third, does it improve end-to-end language-model performance at matched cache rates?

5.1 Per-coordinate MSE on the canonical source

We sample from $f_{d,k}$ for $d \in \{64, 256\}$ and $k \in \{2, 4, 8, 16, 32\}$. Each FIBQUANT codebook is built by Table 2 with $M = 30N$ training samples, $R = 4$ random restarts, and $T_{\text{LM}} = 25$ Lloyd–Max iterations per restart. The scalar baseline is Lloyd–Max quantization of the shifted-Beta marginal with $L = 2^b$ levels.

Figure 3 shows the expected separation. At the integer rates where scalar TURBOQUANT exists, FIBQUANT lies below it. Between those integer rates, FIBQUANT fills the missing fractional-bit operating points. Below one bit per coordinate, scalar random-access quantization has no corre-

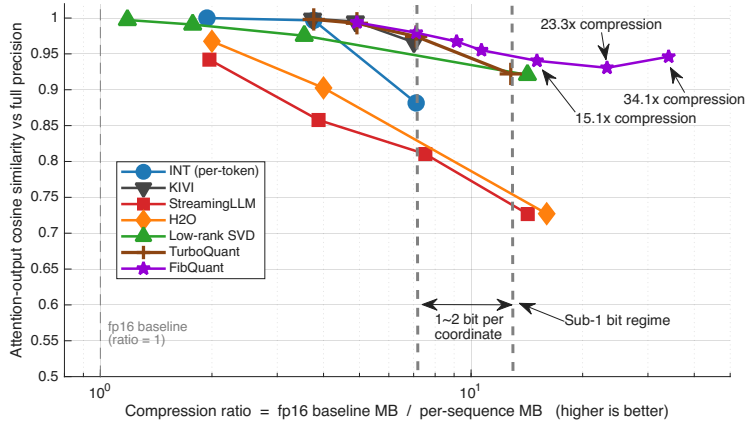


Figure 4: Memory–fidelity Pareto on the real GPT-2 small KV cache (one sequence, $T_{\text{seq}} = 512$). Horizontal axis: compression ratio = (fp16 MB)/(per-seq MB) on a log scale, higher is better. Three guideline ratios are marked: $1\times$ (fp16 baseline), $10.7\times$ (last sub-2-MB scalar-equivalent point), and $34.1\times$ (FIBQUANT’s extreme point at $k = 64$, $N = 16384$). Above $\sim 5\times$, FIBQUANT, TURBOQUANT and KIVI sit on top of one another. Above $10\times$, every non-rotation universal method drops out, and the curve splits into low-rank SVD (calibrated, per-(layer, head)) and FIBQUANT (universal, calibration-free).

sponding point, while vector blocks continue to trade codebook size against rate. Repeating the experiment at $d = 256$ shifts the curves down by the predicted $1/d$ variance scaling.

5.2 Real GPT-2 KV cache

We next evaluate the full KV cache of GPT-2 small ($L = 12$, $H = 12$, $T_{\text{seq}} = 512$, $d = 64$; 18.87MB per sequence at fp16) on 16 WikiText prompts. The comparison includes per-token INT $\{2, 4, 8\}$, KIVI, STREAMINGLLM, H2O, low-rank SVD, scalar TURBOQUANT, and FIBQUANT. For each reconstructed cache \hat{K}, \hat{V} , we run the original softmax attention using 32 random queries and average the per-head output cosine similarity. Memory counts charge all per-vector side information, such as norms and KIVI scales, but amortize shared codebooks and rotations across cached sequences.

Figure 4 has three regimes. Up to about $7\times$ compression, FIBQUANT, TURBOQUANT, and KIVI all preserve attention outputs well; the choice is mainly systems-driven. Between $10\times$ and $25\times$, the non-rotation universal baselines either have no operating point or lose fidelity rapidly, while FIBQUANT continues along a dense curve. Beyond $20\times$, only low-rank SVD and FIBQUANT remain competitive; the distinction is that SVD is calibrated per layer and head, whereas FIBQUANT is universal and fixed-rate. The most compressed FIBQUANT point, $(k, N) = (64, 16384)$, reaches $34.1\times$ compression at 0.946 attention cosine similarity.

Why a full-vector code can win at a lower rate. At $N = 16384$, the $k = d = 64$ point compresses harder than the $k = d/2 = 32$ point ($34.1\times$ versus $23.3\times$) and nevertheless has higher attention fidelity (0.946 versus 0.931). The reason is geometric. With $k = d$, the normalized vector lies exactly on \mathbb{S}^{d-1} , so all bits are spent on angular packing—the same quantity read by attention inner products. With $k = d/2$, the reconstruction is a product of two independently quantized halves and must also spend resolution on radial fluctuations that are less aligned with attention fidelity. The per-vector reconstruction table in Appendix G shows the corresponding cosine improvement, which the softmax amplifies at the attention-output level.

5.3 End-to-end LLM rate–distortion

Finally, we replace the runtime KV cache of TinyLlama-1.1B-Chat-v1.0 (Apache 2.0; $L = 22$, $H_{kv} = 4$, $d = 64$) by $x \mapsto \text{decode}(\text{encode}(x))$. The model therefore uses exactly the reconstructed cache that would be stored in memory. We report sliding-window WikiText-103-raw per-

plexity ($T_{\text{seq}} = 8192$, window 2048, stride 512) and zero-shot HellaSwag accuracy on 200 items. FIBQUANT is evaluated at $b \in \{2, 2.5, 3, 3.5, 4\}$; INT and TURBOQUANT at $b \in \{2, 3, 4\}$.

Table 1: End-to-end rate–distortion on TinyLlama-1.1B (524,288 WikiText-103 tokens, sliding window 2048 / stride 512; 200 HellaSwag items, log-likelihood ranking). At every matched integer rate FIBQUANT (bold) strictly dominates both per-token INT and rotated-scalar TURBOQUANT; at fractional rates only FIBQUANT operates. fp16 reference: ppl = 8.619, HellaSwag = 49.5%.

Codec	b (bits/coord)	Compression	WikiText-103 PPL ↓	HellaSwag (%) ↑
fp16 baseline	—	1×	8.619	49.5
INT $b=4$	4.00	4×	9.244	47.5
INT $b=3$	3.00	5.3×	36.940	37.0
INT $b=2$	2.00	8×	4450.506	22.5
TURBOQUANT $b=4$	4.00	4×	9.220	45.5
TURBOQUANT $b=3$	3.00	5.3×	11.413	46.5
TURBOQUANT $b=2$	2.00	8×	56.717	33.5
FIBQUANT $k=2, N=256$	4.00	4×	8.715	47.5
FIBQUANT $k=2, N=128$	3.50	4.6×	8.881	48.0
FIBQUANT $k=2, N=64$	3.00	5.3×	9.248	47.5
FIBQUANT $k=4, N=1024$	2.50	6.4×	10.219	44.0
FIBQUANT $k=4, N=256$	2.00	8×	15.879	41.5

Table 1 shows the same pattern end-to-end. At matched integer rates, FIBQUANT improves both perplexity and HellaSwag. The gap is modest at $b = 4$, larger at $b = 3$, and decisive at $b = 2$: FIBQUANT obtains 15.88 perplexity, whereas scalar TURBOQUANT reaches 56.72 and per-token INT collapses. The fractional points are equally important. At $b = 3.5$, FIBQUANT is within 0.27 perplexity of fp16; at $b = 2.5$, it provides an intermediate operating point unavailable to scalar fixed-bit codecs. This is the practical value of the dense rate axis: the cache budget can be chosen first, and the codec can be placed exactly on it.

6 Discussion and conclusion

Operating point and implementation. The encoder is a batched nearest-codeword search and the decoder is a table lookup followed by inverse rotation. The shared Pareto library is small—about 5 MB in our implementation—and is amortized across cached sequences. The useful operating regions are clear from Figure 4: full-vector or large-block codes are most attractive in the sub-one-bit regime; $k \in \{4, 8\}$ is effective around one to two bits per coordinate; and $k = 2$ is already sufficient in the higher-rate regime. If strict random access is relaxed, the emitted indices could be entropy-coded using a hyperprior [29]; that extension trades addressability for additional rate reduction and is therefore separate from the fixed-rate codec studied here.

Limitations. The theory identifies the canonical source and the high-rate vector gain, but finite-rate Lloyd–Max optimality for every practical (d, k, N) is not characterized in closed form. The largest end-to-end experiment here uses TinyLlama-1.1B, and the GPT-2 study reports attention-output fidelity rather than full generation quality. Larger models, longer contexts, bootstrap confidence intervals over rotations and prompts, and fused-kernel implementations are natural next steps.

Conclusion. The random-access constraint looks like an engineering detail, but it has a mathematical consequence: after normalization and Haar rotation, every cache block has the spherical-Beta law $f_{d,k}$. Once that source is named, the design becomes classical. Use companding for the radius, quasi-uniform spherical points for the direction, and Lloyd–Max to polish the finite-rate cells. The result keeps the fixed-address interface of scalar rotation codes, recovers vector shaping and density-matching gains, and opens the sub-one-bit regime without calibration. Random access does not preclude good source coding; it tells us which source to code.

References

- [1] B. Jiang, T. Yang, Y. Liu, C. Zhang, X. He, S. Jin. KVComp: A high-performance, LLM-aware, lossy compression framework for KV cache. *arXiv:2509.00579*, 2025.
- [2] Z. Liu, J. Yuan, H. Jin, S. Zhong, Z. Xu, V. Braverman, B. Chen, X. Hu. KIVI: A tuning-free asymmetric 2-bit quantization for KV cache. In *ICML*, 2024.
- [3] C. Hooper, S. Kim, H. Mohammadzadeh, M. W. Mahoney, Y. S. Shao, K. Keutzer, A. Gholami. KVQuant: Towards 10 million context length LLM inference with KV cache quantization. In *NeurIPS*, 2024.
- [4] H. Kang, Q. Zhang, S. Kundu, G. Jeong, Z. Liu, T. Krishna, T. Zhao. GEAR: An efficient KV cache compression recipe for near-lossless generative inference of LLM. *arXiv:2403.05527*, 2024.
- [5] A. Zandieh, M. Daliri, I. Han. QJL: 1-bit quantized JL transform for KV cache quantization with zero overhead. In *AAAI*, 2025.
- [6] A. Zandieh, M. Daliri, M. Hadian, V. Mirrokni. TurboQuant: Online vector quantization with near-optimal distortion rate. In *ICLR*, 2026.
- [7] J. Gao, X. Long, B. Hua, B. Cui, R. Cheng. RaBitQ: Quantizing high-dimensional vectors with a theoretical error bound for approximate nearest neighbor search. In *SIGMOD*, 2024.
- [8] J. Gao, Y. Gou, Y. Xu, J. Shi, Y. Yang, S. Li, R. C.-W. Wong, C. Long. Revisiting RaBitQ and TurboQuant: A symmetric comparison of methods, theory, and experiments. *arXiv:2604.19528*, 2026.
- [9] Z. Zhang, Y. Sheng, T. Zhou, T. Chen, L. Zheng, R. Cai, Z. Song, Y. Tian, C. Ré, C. Barrett, Z. Wang, B. Chen. H2O: Heavy-hitter oracle for efficient generative inference of large language models. In *NeurIPS*, 2023.
- [10] G. Xiao, Y. Tian, B. Chen, S. Han, M. Lewis. Efficient streaming language models with attention sinks. In *ICLR*, 2024.
- [11] Y. Li, Y. Huang, B. Yang, B. Venkitesh, A. Locatelli, H. Ye, T. Cai, P. Lewis, D. Chen. SnapKV: LLM knows what you are looking for before generation. In *NeurIPS*, 2024.
- [12] Z. Cai, Y. Zhang, B. Gao, Y. Liu, Y. Li, T. Liu, K. Lu, W. Xiong, Y. Dong, J. Hu, W. Xiao. PyramidKV: Dynamic KV cache compression based on pyramidal information funneling. *arXiv:2406.02069*, 2024.
- [13] C.-C. Chang, W.-C. Lin, C.-Y. Lin, C.-Y. Chen, Y.-F. Hu, P.-S. Wang, N.-C. Huang, L. Ceze, M. S. Abdelfattah, K.-C. Wu. Palu: Compressing KV cache with low-rank projection. In *ICLR*, 2025.
- [14] T. Dettmers, M. Lewis, Y. Belkada, L. Zettlemoyer. LLM.int8(): 8-bit matrix multiplication for transformers at scale. In *NeurIPS*, 2022.
- [15] J. Max. Quantizing for minimum distortion. *IRE Trans. Information Theory*, 6(1):7–12, 1960.
- [16] S. P. Lloyd. Least squares quantization in PCM. *IEEE Trans. Information Theory*, 28(2):129–137, 1982.
- [17] A. Gersho. Asymptotically optimal block quantization. *IEEE Trans. Information Theory*, 25(4):373–380, 1979.
- [18] R. M. Gray, D. L. Neuhoff. Quantization. *IEEE Trans. Information Theory*, 44(6):2325–2383, 1998.
- [19] J. H. Conway, N. J. A. Sloane. *Sphere Packings, Lattices and Groups*. Springer, 3rd ed., 1999.
- [20] L. Kuipers, H. Niederreiter. *Uniform Distribution of Sequences*. Wiley, 1974.
- [21] H. Niederreiter. *Random Number Generation and Quasi-Monte Carlo Methods*. SIAM, 1992.
- [22] A. González. Measurement of areas on a sphere using Fibonacci and latitude–longitude lattices. *Mathematical Geosciences*, 42(1):49–64, 2010.
- [23] E. B. Saff, A. B. J. Kuijlaars. Distributing many points on a sphere. *The Mathematical Intelligencer*, 19(1):5–11, 1997.
- [24] M. Roberts. The unreasonable effectiveness of quasirandom sequences. Online article, 2018.
- [25] A. Sander. Fibonacci lattices. Online interactive notebook, <https://observablehq.com/@meetamit/fibonacci-lattices>, 2018.
- [26] P. Larsson, L. K. Rasmussen, M. Skoglund. The Golden Quantizer: The complex Gaussian random variable case. *IEEE Wireless Communications Letters*, 7(3):312–315, 2018.
- [27] A. Mojsilović, E. Soljanin. Color quantization and processing by Fibonacci lattices. *IEEE Trans. Image Processing*, 10(11):1712–1725, 2001.
- [28] M. C. Viganó, G. Toso, G. Caille, C. Mangenot, I. E. Lager. Sunflower array antenna with adjustable density taper. *International Journal of Antennas and Propagation*, vol. 2009, Article ID 624035, 2009.
- [29] J. Ballé, D. Minnen, S. Singh, S. J. Hwang, N. Johnston. Variational image compression with a scale hyperprior. In *ICLR*, 2018.

A Codebook construction algorithm

Table 2 gives the full pseudocode for the FIBQUANT codebook construction described in Sec. 3.3: Beta-quantile radii, quasi-uniform directions, and multi-restart Lloyd–Max polish, together with the large- d shortcut from Appendix D that replaces the radial law by the typical shell.

Table 2: FIBQUANT codebook construction (Beta-quantile radii, quasi-uniform directions, Lloyd–Max polish).

Input: block size k , codebook size N , ambient dimension d , training set size M , restarts R , Lloyd–Max iterations T_{LM} .

Output: refined codebook $\mathcal{C}^* \subset \mathbb{B}^k$.

- 1: Set $\beta_{d,k} \leftarrow \frac{k}{k+2} \cdot \frac{d-k-2}{2} + 1$.
- 2: **for** $n = 1, \dots, N$ **do**
- 3: $q_n \leftarrow (n - \frac{1}{2})/N$.
- 4: **if** $k = 2$ **then** $r_n \leftarrow \sqrt{1 - (1 - q_n)^{4/d}}$ // closed form
- 5: **else** $r_n \leftarrow \sqrt{\text{BetaInv}(q_n; k/2, \beta_{d,k})}$.
- 6: **end for**
- 7: Generate quasi-uniform directions $\{u_n\}_{n=1}^N$ on \mathbb{S}^{k-1} (Fibonacci spiral, Fibonacci sphere, or Roberts–Kronecker).
- 8: Initialize $\mathcal{C}^{(0)} \leftarrow \{r_n u_n\}_{n=1}^N$.
- 9: Sample $X = \{x_i\}_{i=1}^M$ from $f_{d,k}$ (or collect calibrated rotated KV blocks).
- 10: $\mathcal{C}^* \leftarrow \mathcal{C}^{(0)}$, $D^* \leftarrow \infty$.
- 11: **for** $j = 1, \dots, R$ **do** // multi-restart
- 12: Rotate $\mathcal{C}^{(0)}$ by a random orthogonal $\Omega_j \in \mathbb{R}^{k \times k}$ to get \mathcal{C} .
- 13: **for** $t = 1, \dots, T_{\text{LM}}$ **do**
- 14: Assign each x_i to its nearest codeword in \mathcal{C} ;
- 15: update each occupied codeword to the assigned centroid;
- 16: repair empty cells by splitting a high-distortion donor.
- 17: **end for**
- 18: **if** $D(\mathcal{C}) < D^*$ **then** $\mathcal{C}^* \leftarrow \mathcal{C}$, $D^* \leftarrow D(\mathcal{C})$.
- 19: **end for**
- 20: **return** \mathcal{C}^* .

Large- d shortcut (Appendix D): replace lines 1–6 by $r_n \leftarrow \bar{R} = \sqrt{k/d}$ for all n , then continue from line 7.

B Proof of Lemma 1 and Theorem 2

Spherical-Beta vector marginal (Lemma 1). Let $G \sim \mathcal{N}(0, I_d)$ and $U = G/\|G\|$, Haar-uniform on \mathbb{S}^{d-1} . At any $x \in \mathbb{B}^k$, the remaining $d - k$ coordinates lie on a sphere of radius $\sqrt{1 - \|x\|^2}$ in dimension $d - k - 1$, with surface area $\propto (1 - \|x\|^2)^{(d-k-2)/2}$. The polar normalization $\int_{\mathbb{B}^k} (1 - \|x\|^2)^\alpha dx = \pi^{k/2} \Gamma(\alpha+1)/\Gamma(\alpha+k/2+1)$ with $\alpha = (d-k-2)/2$ gives the constant $C_{d,k}$. In polar coordinates $x = ru$ the angular measure factors out and r has density $\propto r^{k-1}(1-r^2)^{(d-k)/2-1}$; the change of variables $z = r^2$ yields $R^2 \sim \text{Beta}(k/2, (d-k)/2)$. Specializing to $k = 1$ recovers the shifted-Beta coordinate marginal $f_{d,1}(x) \propto (1-x^2)^{(d-3)/2}$ used by scalar TURBOQUANT, with $\mathbb{E}X = 0$ and $\text{Var}(X) = 1/d$.

Vector-code dominance (Theorem 2). A scalar product code on k coordinates is a k -vector quantizer whose codebook is the Cartesian product \mathcal{A}^k of L_{sc} scalar levels; the optimal k -vector quantizer minimizes MSE over a strictly larger class, so $D_{\text{FQ}}^* \leq D_{\text{sc}}$, with equality iff the optimum is a product (only at $k = 1$). For the high-rate decomposition, Bennett’s distortion integral gives $D_{\text{sc}}(d, b) \sim G_1 2^{-2b} I_{d,1}(1/3)^3$ per coordinate, hence $k G_1 2^{-2b} I_{d,1}(1/3)^3$ for k coordinates. Gersho’s high-rate VQ result [17] gives $D_{\text{FQ}}^{\text{vec}}(d, k, b) \sim G_k^* 2^{-2b} I_{d,k}(k/k+2)^{(k+2)/k}$ per vector; dividing by k and taking the ratio yields (8). Both factors are ≥ 1 .

C Large- d finite-rate behavior

The high-rate decomposition takes $N \rightarrow \infty$ with (d, k) fixed; in serving, d is also large.

Theorem 3 (Large- d finite-rate RD). *Let $X = RU$ as in Lemma 1. (i) Fixed k , $d \rightarrow \infty$: $\sqrt{d}X \Rightarrow Z \sim \mathcal{N}(0, I_k)$, and for every fixed N , $d \cdot D_{d,k,N}^* \rightarrow \inf_{|c| \leq N} \mathbb{E}_Z \min_{c \in \mathcal{C}} \|Z - c\|^2$. (ii) Proportional regime, $k/d \rightarrow \rho \in (0, 1)$: $R^2 \rightarrow \rho$ in probability, and for the fixed-shell codebook $\mathcal{C}_N = \{\sqrt{\rho} v_i\}_{i=1}^N$ with directions $v_i \in \mathbb{S}^{k-1}$, $D_{d,k,N}(\mathcal{C}_N) = 2\rho \mathbb{E}_U [1 - \max_v \langle U, v \rangle] + o(1)$. Under the equal-cap heuristic with $N = 2^{bk}$ and $t_b = \sqrt{1 - 2^{-2b}}$, the asymptotic shell distortion is $2\rho(1 - t_b)$ for fixed-radius caps and $\rho 2^{-2b}$ for Lloyd-centroid caps.*

The proof reduces to the central limit theorem in (i) and to weak convergence of the radial CDF plus an equal-cap measure argument in (ii). Regime (i) cautions against asymptotic intuition for the small vector sizes used in KV caches; regime (ii) confirms that once k scales with d , the only design problem is angular packing on \mathbb{S}^{k-1} , where Fibonacci-type direction sets are natural.

D Large- d simplification of the radial design

The radial spread of $f_{d,k}$ has standard deviation $\text{sd}(R) \approx (2\sqrt{d})^{-1}$ around the typical radius $\bar{R} = \sqrt{k/d}$. As d grows the source concentrates on an ever-thinner shell, and the Beta-quantile radial design collapses to a single-radius design: the Lloyd-polished single-shell codebook $\mathcal{C}_d^{\text{shell}} = \{\bar{R} u_n\}_{n=1}^N$ has the same finite-rate optimum as the Beta-quantile codebook $\mathcal{C}_d^{\text{Beta}}$, with the difference vanishing at $O(1/d)$ in normalized MSE. Use (5) at moderate d ; use the single-shell init at large d with the same Lloyd polish.

E Fibonacci sphere and the multi-shell codebook at $k = 3$

This appendix gives the angular construction at $k = 3$ in two stages: *single-shell* (uniform angular quantization at one fixed radius) and *multi-shell* (composing several Beta-quantile radii with one Fibonacci-sphere direction set per shell). Together they specify the deterministic 3D codebook that FIBQUANT Lloyd-polishes before deployment.

Single-shell Fibonacci sphere: uniform angular quantization. On the unit sphere \mathbb{S}^2 the Fibonacci sphere places M_a codewords at equal-area latitude bands times golden-angle azimuth [25, 22]:

$$z_n = 1 - \frac{2n-1}{M_a}, \quad \theta_n = 2\pi(n-1)(1-1/\varphi), \quad u_n = (\sqrt{1-z_n^2} \cos \theta_n, \sqrt{1-z_n^2} \sin \theta_n, z_n), \quad (10)$$

where $\varphi = (1 + \sqrt{5})/2$ is the golden ratio. The latitude choice $z_n = 1 - (2n-1)/M_a$ gives bands of equal area $4\pi/M_a$, and the golden-angle azimuth ensures the in-band azimuthal positions form a low-discrepancy 1D sequence (the fractional parts of n/φ have discrepancy $O(\log M_a/M_a)$, the optimal rate among 1D sequences). The result is a tessellation of \mathbb{S}^2 in which every Voronoi cell has area $\approx 4\pi/M_a$ and aspect ratio close to one — the geometric property that makes (10) the right deterministic init for any single-shell angular code on \mathbb{S}^2 . Figure 5 visualizes the codewords on \mathbb{S}^2 for $M_a \in \{32, 64, 128, 256\}$.

Multi-shell extension: composing radii with directions. The construction in Sec. 3.3 places every codeword on its own Beta-quantile radius — that is, N distinct shells with one direction per shell. At $k = 3$ this is wasteful because directional packing on \mathbb{S}^2 has its own resolution limit: the single-shell Fibonacci sphere of (10) already tiles \mathbb{S}^2 with angular spacing $\approx 1/\sqrt{M_a}$. We therefore parameterize the codebook as a *multi-shell* construction

$$\mathcal{C}(S, M_a) = \bigcup_{s=1}^S \{ \tilde{r}_s u_n^{(s)} : n = 1, \dots, M_a \}, \quad N = S \cdot M_a, \quad (11)$$

with $\tilde{r}_s = \sqrt{\text{BetaInv}(q_s; k/2, \beta_{d,k})}$ at $q_s = (s - \frac{1}{2})/S$ and $\{u_n^{(s)}\}_{n=1}^{M_a}$ a fresh Fibonacci-sphere direction set per shell. At fixed budget $N = S \cdot M_a$ the design problem reduces to a one-dimensional

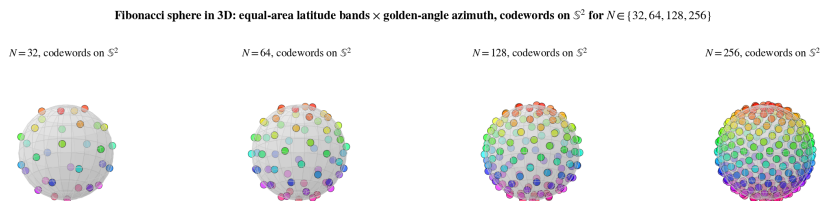


Figure 5: Fibonacci sphere of M_a codewords on S^2 for $M_a \in \{32, 64, 128, 256\}$, shown in orthographic projection from a fixed viewpoint. Equal-area latitude bands times golden-angle azimuth give Voronoi cells of area $\approx 4\pi/M_a$ and unit aspect ratio.

search over the integer factorization (S, M_a) that minimizes training MSE. In practice the optimum lies at $S \approx \mathcal{O}(d^{1/3})$ for $k = 3$ and is found by exhaustive enumeration of all factor pairs in $\mathcal{O}(\sqrt{N})$ time before the Lloyd–Max polish. At moderate d this yields up to 0.3 dB lower training MSE at $k = 3$ for the rate range studied here. At $k \geq 4$ the same multi-shell template is used with the single-shell direction set replaced by the Roberts–Kronecker rank-one sequence $\xi_{n,j} = \{(n - \frac{1}{2}) \phi_k^{-j}\}$ where ϕ_k is the positive real root of $\phi^{k+1} = \phi + 1$. Figure 6 visualizes the construction explicitly at $d = 64, L = 4, M_a = 32$ ($N = 128$): each individual shell is shown alone in the top row, and the combined codebook is shown in 3D below.

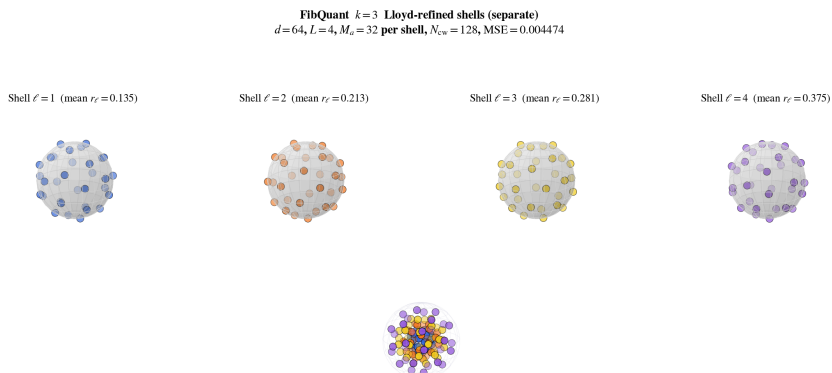


Figure 6: FIBQUANT $k = 3$ Lloyd-refined multi-shell codebook (11) at $d = 64, L = 4$ shells, $M_a = 32$ codewords per shell ($N_{\text{cw}} = 128$). **Top row:** each shell $\ell = 1, \dots, 4$ shown alone as $M_a = 32$ Fibonacci-sphere codewords scaled by the per-shell Beta-quantile radius r_ℓ and Lloyd-polished against Haar samples on that shell. **Bottom:** all four shells overlaid in 3D, with a faint wireframe at the outermost shell radius for context. Per-shell radii are $r_1 \approx 0.117, r_2 \approx 0.201, r_3 \approx 0.265, r_4 \approx 0.330$, sorted from inside to outside. The “separate” Lloyd polish — each shell refined independently against samples on its own typical shell — recovers most of the multi-shell gain at a fraction of the cost of joint Lloyd over all $N = 128$ codewords.

F Sub-linear encoder complexity for large N : hierarchical list decoding

The naive FIBQUANT encoder for one k -vector is one batched dot-product against the N codewords, costing $\mathcal{O}(Nk)$ FLOPs per block and $\mathcal{O}(dN)$ per cached vector. At the most aggressive operating points used in the paper ($k = 64, N = 16384$ at $d = 64$) this is $\sim 10^6$ FLOPs per cached vector — still cheap on a GPU, but the linear-in- N scaling becomes the dominant decode-time cost when N grows. This appendix sketches two complexity-reduction ideas that reduce the encoder cost from $\mathcal{O}(N)$ to $\mathcal{O}(\sqrt{N})$ per k -block while preserving the bitstream and the random-access decoder interface. Decoding is unaffected — it remains a single table lookup per index.

Stage 1: radius-first search. The multi-shell construction (11) writes $\mathcal{C} = \bigcup_{\ell=1}^L \{r_\ell u_n^{(\ell)}\}_{n=1}^{M_a}$ with L Beta-quantile radii and $M_a = N/L$ direction codewords per shell. Encoding can exploit this factorization:

1. compute $\rho = \|y^{(m)}\|_2$ once and find $\ell^* = \arg \min_\ell |\rho - r_\ell|$ in $O(L)$ scalar comparisons;
2. search the angular code on shell ℓ^* alone: $\hat{n} = \arg \min_n \|y^{(m)} - r_{\ell^*} u_n^{(\ell^*)}\|^2$ in $O(M_a) = O(N/L)$ inner products.

The total cost is $O(L + N/L)$, minimized at $L = \sqrt{N}$ with total work $\Theta(\sqrt{N})$ per k -block. At $(k, N) = (32, 8192)$ this is roughly $L = M_a \approx 90$ versus $N = 8192$, an $\sim 90\times$ FLOP reduction at the encoder. The trade-off is a small bias: the r_ℓ -nearest shell may not contain the (ru) -nearest codeword when ρ falls between two shells. In the rate range studied here the resulting MSE penalty is below 0.1 dB on the canonical $f_{d,k}$ source.

Stage 2: hierarchical direction code (list decoding). For $k > 3$ the per-shell direction code itself can be restructured into a two-level tree, in the spirit of classical tree-structured vector quantization [18]. Cluster the M_a direction codewords on \mathbb{S}^{k-1} into K parent groups by k -means or by a Roberts–Kronecker partition; let $\mu_j \in \mathbb{S}^{k-1}$ be the mean direction of group j , and \mathcal{G}_j the indices of its M_a/K children. Encoding a direction v proceeds in two stages:

1. compare v against the K parent centroids $\{\mu_j\}_{j=1}^K$ and keep the top- T matches by inner product, forming a candidate list $\mathcal{L}(v)$ of size $T \cdot M_a/K$;
2. search exhaustively within $\mathcal{L}(v)$ for the nearest sub-codeword.

The total work is $O(K + T \cdot M_a/K)$, minimized at $K = \sqrt{TM_a}$ with cost $\Theta(\sqrt{TM_a})$. The list size T controls the accuracy / complexity trade-off: $T = 1$ is greedy nearest-cluster decoding (fast, occasionally suboptimal), while $T = K$ recovers the exhaustive search. For Fibonacci-sphere/Roberts–Kronecker direction sets the parent clusters are themselves quasi-uniform on \mathbb{S}^{k-1} , so the event “the true nearest codeword’s parent is not in the top- T list” has probability that decays geometrically in T .

Composition. Composing both stages, the per- k -block cost becomes $O(L + K + TM_a/K)$. At $L = K = \sqrt{N/T}$ this is $\Theta(\sqrt{TN})$ FLOPs per block, against $\Theta(N)$ for the naive encoder. The bitstream is unchanged: the encoder still emits one index in $\{1, \dots, N\}$ per block, formed as the pair (ℓ^*, \hat{n}) with affine offset $\ell^* \cdot M_a + \hat{n}$; random-access addressing is preserved. The decoder is therefore unchanged, and a downstream consumer (e.g. a fused attention kernel) cannot tell whether the encoder used the naive search or the hierarchical one. The cost is paid only on the cache-write path, which already runs once per token, while the decode path — which runs T_{seq} times per query and is the actual bandwidth bottleneck — is identical in either case.

G Per-vector reconstruction fidelity on the GPT-2 small KV cache

Table 3 complements the attention-output cosine similarity of Figure 4 with two per-vector reconstruction metrics, averaged across all $12 \cdot 12 \cdot T_{\text{seq}} = 73,728$ KV vectors of one GPT-2 small sequence: per-vector cosine similarity $\overline{\text{cos}}(x, \hat{x})$ and normalized reconstruction MSE $\text{NMSE} = 10 \log_{10}(\|x - \hat{x}\|^2 / \|x\|^2)$ in dB. Both reconstruction metrics track $\overline{\text{cos}}_{\text{attn}}$ monotonically; TURBO-QUANT at $b = 4$ recovers vectors at $\overline{\text{cos}} = 0.996$ (−20.4 dB), and FIBQUANT at $b = 0.22$ still preserves $\overline{\text{cos}} \approx 0.80$ (−5.7 dB) — low at the vector level, but enough downstream fidelity to keep attention outputs at 0.946 cosine similarity versus full precision.

Table 3: Per-vector reconstruction fidelity on the GPT-2 small KV cache (one sequence). Per-coord rate b , per-vector $\overline{\cos}(x, \hat{x})$ (\uparrow), NMSE in dB (\downarrow), and attention-output cosine similarity $\overline{\cos}_{\text{attn}}$ (\uparrow).

Method	Operating point	b	$\overline{\cos}(x, \hat{x}) \uparrow$	NMSE (dB) \downarrow	$\overline{\cos}_{\text{attn}} \uparrow$
TURBOQUANT	$b = 4$	4.000	0.996	-20.40	0.998
TURBOQUANT	$b = 3$	3.000	0.984	-14.79	0.993
TURBOQUANT	$b = 2$	2.000	0.942	-9.42	0.974
FIBQUANT	$k = 2, N = 64$	3.000	0.986	-15.34	0.994
FIBQUANT	$k = 4, N = 256$	2.000	0.951	-10.19	0.980
FIBQUANT	$k = 8, N = 4096$	1.500	0.916	-8.08	0.967
FIBQUANT	$k = 8, N = 1024$	1.250	0.880	-6.56	0.955
FIBQUANT	$k = 8, N = 256$	1.000	0.828	-5.07	0.937
FIBQUANT	$k = 16, N = 4096$	0.750	0.805	-5.21	0.933
FIBQUANT	$k = 16, N = 8192$	0.812	0.811	-5.47	0.940
FIBQUANT	$k = 64, N = 16384$	0.219	0.795	-5.74	0.946